Recent results from the LHCf experiment

G. Mitsuka*on behalf of the LHCf Collaboration

Solar-Terrestrial Environment Laboratory, Nagoya University

Abstract

The Large Hadron Collider forward experiment measured very forward neutral particle spectra in LHC proton-proton collisions in early 2010. In this paper we will discuss the energy spectra of photon and transverse momentum spectra of neutral pion at the 7 TeV proton-proton collision, and the inclusive photon energy spectra taken at the 900 GeV collisions. The spectra in both collision energies are also compared with the predictions of several hadronic interaction models that are often used for high energy particle physics and for modeling ultrahigh-energy cosmic ray showers.

1 Introduction

The Large Hadron Collider forward (LHCf) experiment [1] has been designed to measure the hadronic production cross sections of neutral particles emitted in very forward angles in proton-proton collisions at the LHC, including zero degrees. The LHCf detectors have the capability for precise measurements of forward high-energy inclusive-particle-production cross sections of photons, neutrons, and possibly other neutral mesons and baryons. The analyses in this paper concentrate on obtaining (1) the inclusive production rate for π^0s in the rapidity range larger than $y = 8.9$ as a function of the π^0 transverse momentum, and (2) the inclusive production rate for photons in the rapidity ranges $\eta > 8.77$ at 900 GeV and $\eta > 8.81$ at 7 TeV as a function of the photon energy.

This work is motivated by an application to the understanding of ultrahigh-energy cosmic ray (UHECR) phenomena, which are sensitive to the details of soft π^0 and photon production at extreme energy. It is known that the lack of knowledge about forward particle production in hadronic collisions hinders the interpretation of observations of UHECR [2, 3]. Although UHECR observations have made notable advances in the last few years [4–10], critical parts of the analysis depend on Monte Carlo (MC) simulations of air shower development that are sensitive to the choice of the hadronic interaction model.

This paper is organized as follows. In Sec. 2 the LHCf detectors are described. Section 3 summarizes the conditions for taking data and Sec. 4 summarizes the MC simulation methodology. In Sec. 5 the analysis framework is described. The analyses results are then presented in Sec. 6, Sec. 7, and Sec. 8. Finally, concluding remarks are found in Sec. 9.

2 The LHCf detectors

Two independent LHCf detectors, called Arm1 and Arm2, have been installed in the instrumentation slots of the target neutral absorbers (TANs) [11] located ± 140 m from the ATLAS interaction point (IP1) and at zero degree collision angle. Figure 1 shows schematic views of the Arm1 (left) and Arm2 (right) detectors. Inside a TAN the beam-vacuum-chamber makes a Y-shaped transition from a single common beam tube facing IP1 to two separate beam tubes

---

*e-mail: Gaku.Mitsuka@cern.ch

joining to the arcs of the LHC. Charged particles produced at IP1 and directed towards the TAN are swept aside by the inner beam separation dipole magnet D1 before reaching the TAN. Consequently only neutral particles produced at IP1 enter the LHCf detector. At this location the LHCf detectors cover the pseudorapidity range from 8.7 to infinity for zero degree beam crossing angle. With a maximum beam crossing angle of $140\,\mu$rad, the pseudorapidity range can be extended to 8.4 to infinity.

Each LHCf detector has two sampling and imaging calorimeters composed of 44 radiation lengths (X_0) of tungsten and 16 sampling layers of 3 mm thick plastic scintillator. The transverse sizes of the calorimeters are $20 \times 20\,\mathrm{mm}^2$ and $40 \times 40\,\mathrm{mm}^2$ in Arm1, and $25 \times 25\,\mathrm{mm}^2$ and $32 \times 32\,\mathrm{mm}^2$ in Arm2. The smaller and larger calorimeters are called as "small tower" and "large tower", respectively. The small towers cover zero degree collision angle. Four X-Y layers of position sensitive detectors are interleaved with the layers of tungsten and scintillator in order to provide the transverse positions of the showers. Scintillating fiber (SciFi) belts are used for the Arm1 position sensitive layers and silicon micro-strip sensors are used for Arm2. Readout pitches are 1 mm and 0.16 mm for Arm1 and Arm2, respectively.
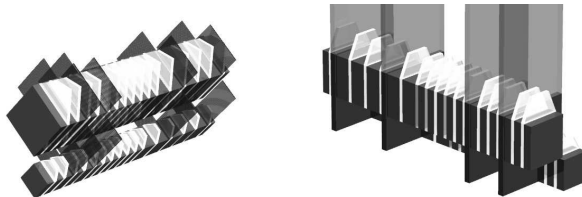

Figure 1: (color online). Schematic views of the Arm1 (left) and Arm2 (right) detectors. The transverse sizes of the calorimeters are $20 \times 20\,\mathrm{mm}^2$ and $40 \times 40\,\mathrm{mm}^2$ in Arm1, and $25 \times 25\,\mathrm{mm}^2$ and $32 \times 32\,\mathrm{mm}^2$ in Arm2.

3 Summary of the conditions for taking data

3.1 proton-proton collisions at $\sqrt{s}$=7 TeV

The experimental data used for the π^0 analysis of this paper were obtained on May 15 and 16, 2010, during proton-proton collisions at $\sqrt{s}$=7 TeV with zero degree beam crossing angle (LHC Fill 1104). Data taking was carried out in two different runs: the first run was on May 15 from 17:45 to 21:23, and the second run was on May 16 from 00:47 to 14:05. The events that were recorded during a luminosity optimization scan and a calibration run were removed from the data set for this analysis. The photon analysis is based on the data of the first run.

The range of total luminosity of the three crossing bunch pairs was $\mathcal{L} = (6.3 - 6.5) \times 10^{28}\mathrm{cm}^{-2}\mathrm{s}^{-1}$ for the first run and $\mathcal{L} = (4.8-5.9)\times 10^{28}\mathrm{cm}^{-2}\mathrm{s}^{-1}$ for the second run. These ranges of luminosity were ideal for the LHCf data acquisition system. The integrated luminosities for the data analysis reported in this paper were derived from the counting rate of the LHCf Front Counters [12], and were $2.53\,\mathrm{nb}^{-1}$ (Arm1) and $1.90\,\mathrm{nb}^{-1}$ (Arm2) after taking the live time percentages into account. The average live time percentages for the first/second run were 85.7 %/81.1 % for Arm1 and 67.0 %/59.7 % for Arm2. The live time percentages for the second run were smaller than the first run owing to a difference in the trigger schemes. In both runs the trigger efficiency achieved was >99% for photons with energy $E > 100\,\mathrm{GeV}$ [13].

The events containing more than one collision in a single bunch crossing (pile-up events) could potentially cause a bias in the p_T spectra. For example combinatorial single-hits from different collisions within a single bunch crossing might be identified as multi-hit events from a single collision and removed from the analysis. However considering that the acceptance of

the LHCf calorimeter for inelastic collisions is $\sim$0.03, only 0.2% of events have more than one shower event in a single calorimeter due to pile-up and this is negligible.

3.2 proton-proton collisions at $\sqrt{s}$=900 GeV

The data sets used in the photon analysis were taken on 2, 3 and 27 May 2010 during the LHC operations with proton-proton collisions at $\sqrt{s} = 900$ GeV, which correspond to the LHC fill identification numbers (Fill ID) 1068, 1069 and 1128, respectively. In these fills, the LHC operated with one crossing bunch and one non-crossing bunch at IP1 in Fill IDs 1068 and 1069 and with four crossing bunches and three non-crossing bunches at IP1 in Fill ID 1128. The luminosity $\mathcal{L}$ at IP1 during these fills was measured by the ATLAS experiment [14]. The luminosity during Fill ID 1068 and 1069 were $\mathcal{L} = 8 - 3 \times 10^{27}$ cm^{-2}s^{-1} and $\mathcal{L} = 12 - 4 \times 10^{27}$ cm^{-2}s^{-1}, respectively. The total luminosity of the four crossing bunches in Fill ID 1128 was approximately $\mathcal{L} = 8 \times 10^{27}$ cm^{-2}s^{-1}. The total integrated luminosity $\int \mathcal{L}dt$ during the LHCf operations in the three fills was 0.30 nb^{-1}. The uncertainty of the luminosity determination is ± 21 % [14]. The inelastic cross-section σ_{inel} for a $\sqrt{s} = 900$ GeV proton-proton collision was estimated to be $\sigma_{inel} = 53.0$ mb from the predictions of the total cross-section and the elastic cross section, which are based on the recent experimental results [15, 16]. The number of inelastic collisions N_{inel} during the three fills was calculated to be 1.58×10^7. The average DAQ live times during the LHCf $\sqrt{s} = 900$ GeV operations was 99.2 % (Arm1) and 98.0 % (Arm2). Because of the very low luminosity and the low event rate per inelastic collision, the probability of the pile-up of events was $< 10^{-4}$, negligibly small.

4 Summary of the methodology for performing Monte Carlo simulations

MC simulation consists of three steps: (1) proton-proton interaction event generation at IP1, (2) transport from IP1 to the LHCf detectors and (3) the response of the LHCf detectors.

Proton-proton interaction events at $\sqrt{s} = 7$ TeV and $\sqrt{s} = 900$ GeV and the resulting flux of secondary particles and their kinematics are simulated with COSMOS [17] (version 8.81). COSMOS acts as the front end for the external hadronic interaction models (QGSJET II-03 [18], DPMJET 3.04 [19], SIBYLL 2.1 [20], and EPOS 1.99 [21]) that describe the proton-proton interactions. While for PYTHIA 8.145 [22, 23], proton-proton interaction events are simulated by PYTHIA 8.145 standalone.

Next, the generated secondary particles are transported in the beam pipe from IP1 to the TAN, taking account of the deflection of charged particles by the Q1 quadrupole and D1 beam separation dipole, particle decay, and particle interaction with the beam pipe and the Y-shaped beam-vacuum-chamber transition made of copper ($1 X_0$ projected thickness in front of the LHCf detectors). Charged particles are swept away by the D1 magnet before reaching the LHCf detectors. This simulation uses the EPICS library [17] (version 7.49) and a part of COSMOS.

Finally the simulations of the showers produced in the LHCf detectors and their response are carried out for the particles arriving at the TAN using the COSMOS and EPICS libraries. The survey data for detector position and random fluctuations equivalent to electrical noise are taken into account in this step. The Landau-Pomeranchuk-Migdal effect [24, 25] that longitudinally lengthens an electromagnetic shower at high energy is also considered.

5 Analysis framework

5.1 Multi-hit selection

As noted later, an energy reconstruction relies on the sum of the visible-energy-deposits on each scintillator layer. Hence, in the case of multiple hits on one tower (multi-hit), the energy of each entering particle can not be reconstructed individually, then such misreconstruction possibly causes the incorrect energy spectrum. Therefore the multi-hit selection is crucial in the data analysis in LHCf. The multi-hit selection is based on the peak-finding algorithm that has been implemented in the TSpectrum [26] class in ROOT [27].

According to the estimation with the MC simulations, single-hit events can be collected with the efficiency larger than 98 % and its energy dependence is less than 2 %. Also the efficiency has no significant dependence on the PID criteria.

5.2 Reconstruction of shower position

Determination of the incidence position of entering particles on the detector is one of the most important reconstruction processes for two reasons:

- Because of the small size of calorimeter, a part of particle shower is unavoidably leaked out from the calorimeter. Shower leakage can be compensated by adding the corresponding energy deposit which can vary as a function of incidence position.

- Invariant mass of two photons decayed from π^0 can be reconstructed by the energy on each tower and opening angle. Opening angle is geometrically determined in terms of the incidence positions on each tower and the distance between the decay point of π^0 and the detector.

Energy deposit along the lateral direction is fitted by Eq.(1), and the fitted variable b is the reconstructed incidence position.

$$f(a, b, c) \propto c \frac{a}{[(x - b)^2 + a]^{3/2}}. \tag{1}$$

Best-fit values of a, b and c are extracted by minimizing the χ^2 function (i.e., a goodness-of-fit test) using the MINOS-MINUIT algorithm [28]. The estimated resolution using the toy MC simulations and test beam data for a single photon with energy $E > 100$ GeV is better than $200\,\mu$m and $100\,\mu$m for Arm1 and Arm2, respectively [29, 30].

5.3 Shower leakage correction

A part of shower developed in the detector is unavoidably leaked out from the calorimeter because of its small lateral size (in the case of tungsten, the Moliere radius is about 9 mm). The fraction of leakage can be geometrically estimated by the MC simulation for each incidence position. Events with the particles hitting on the outer 2 mm from the calorimeter edge are not used in the analysis because of the difficulty to compensate the large amount of shower leakage.

Another aspect of the shower leakage is that leaked to the other side of tower (i.e. leakage-in) which has the impact in the reconstruction of π^0 mass, in which the sensitivity and resolution rely on the precise reconstruction of the energy of the pair of two photons.

5.4 Energy reconstruction

Shower energy is reconstructed using the visible-energy-deposit on the calorimeter. Thanks to the sufficiently dense absorber made by tungsten (totally $44\,X_0$), the longitudinal development of electromagnetic shower can be perfectly detected, while that of hadronic shower can be partially leaked out from the last layer of the scintillators.

Sum of the energy deposits (called as *SumdE*) in units of MIP is defined as

$$SumdE = \sum_{i=2}^{11} E_{dep}^i + 2\sum_{i=12}^{13} E_{dep}^i \tag{2}$$

where index i denotes the i-th scintillator. Coefficient 2 in the second term corresponds to the twice longer tungsten-absorber ($4\,X_0$ for each layer) layers than that in the former layers ($2\,X_0$ for each layer). The energy deposit in the 1st layer is disregarded in the energy reconstruction since this layer is highly influenced by the background events induced by collisions between beam and residual gas. Conversion constants from *SumdE* to reconstructed energy are determined by the MC simulation from the energy threshold up to $3.5\,\text{TeV}$.

5.5   Particle identification

Particle identification (PID) is one of the important processes executed in the data analysis, especially both purity and efficiency must be addressed. If only keeping higher purity is focused, the efficiency may fall down because of the severe cut and vice versa.

Among many proposed approaches, the $L_{90\%}$ method is employed in the current data analysis. This method is based on the shower development along the longitudinal direction, where an electromagnetic shower may develop faster than a hadronic shower.

$L_{90\%}$ is defined as the shower depth in units of X_0 where an integral of energy deposits in the calorimeter from $0\,X_0$ to $L_{90\%}$ achieves $90\,\%$ of the total energy deposit as described in Eq.(3).

$$\int_0^{L_{90\%}} E_{dep} = 0.9 \int_0^{44\,X_0} E_{dep} \tag{3}$$

6   Results of π^0 analysis at $\sqrt{s} = 7\,\text{TeV}$

The combined p_T spectra of the Arm1 and Arm2 detectors are presented in Fig. 3 for six ranges of rapidity y: 8.9 to 9.0, 9.0 to 9.2, 9.2 to 9.4, 9.4 to 9.6, 9.6 to 10.0, and 10.0 to 11.0. The spectra in Fig. 3 are after all corrections discussed in previous sections have been applied. The inclusive production rate of neutral pions is given by the expression

$$\frac{1}{\sigma_\text{inel}} E \frac{d^3\sigma}{dp^3} = \frac{1}{N_\text{inel}} \frac{d^2 N(p_\text{T}, y)}{2\pi \cdot p_\text{T} \cdot dp_\text{T} \cdot dy}. \tag{4}$$

σ_inel is the inelastic cross section for proton-proton collisions at $\sqrt{s} = 7\,\text{TeV}$. $Ed^3\sigma/dp^3$ is the inclusive cross section of π^0 production. The number of inelastic collisions, N_inel, used for normalizing the production rates of Fig. 3 has been calculated from $N_\text{inel} = \sigma_\text{inel} \int \mathcal{L}dt$, assuming the inelastic cross section $\sigma_\text{inel} = 73.6\,\text{mb}$. This value for σ_inel has been derived from the best COMPETE fits [16] and the TOTEM result for the elastic scattering cross section [15]. Using the integrated luminosities reported in Sec. 3.1, N_inel is 1.85×10^8 for Arm1 and 1.40×10^8 for Arm2. $d^2 N(p_\text{T}, y)$ is the number of π^0s detected in the transverse momentum interval (dp_T) and the rapidity interval (dy) with all corrections applied. In Fig. 3, the $68\,\%$ confidence intervals incorporating the statistical and systematic uncertainties are indicated by the shaded green rectangles.

For comparison, the p_T spectra predicted by various hadronic interaction models are also shown in Fig. 3. The hadronic interaction models that have been used in Fig. 3 are DPMJET 3.04 (solid, red), QGSJET II-03 (dashed, blue), SIBYLL 2.1 (dotted, green), EPOS 1.99 (dashed dotted, magenta), and PYTHIA 8.145 (default parameter set, dashed double-dotted, brown). In these MC simulations, π^0s from short lived particles that decay within $1\,\text{m}$ from IP1, for example $\eta \to 3\pi^0$, are also counted to be consistent with the treatment of the experimental

data. Note that, since the experimental p_T spectra have been corrected for the influences of the detector responses, event selection efficiencies and geometrical acceptance efficiencies, the p_T spectra of the interaction models may be compared directly to the experimental spectra as presented in Fig. 3.

Among hadronic interaction models tested in this analysis, EPOS 1.99 shows the best overall agreement with the LHCf data. However EPOS 1.99 behaves softer than the data in the low p_T region, $p_T \lesssim 0.4\,\mathrm{GeV}$ in $9.0 < y < 9.4$ and $p_T \lesssim 0.3\,\mathrm{GeV}$ in $9.4 < y < 9.6$, and behaves harder in the large p_T region. Specifically a dip found in the ratio of EPOS 1.99 to the LHCf data for $y > 9.0$ can be attributed to the transition between two pion production mechanisms: string fragmentation via cut Pomeron process (low energy $\sim$ low p_T for the fixed rapidity) and remnants of projectile/target (high energy $\sim$ large p_T for the fixed rapidity) [31].

7   Results of photon analysis at $\sqrt{s} = 7\,\mathrm{TeV}$

Considering the difference of the detector structures between two arms, events fallen in the common rapidity and azimuthal ranges are selected. The ranges for the small calorimeters and the large calorimeters are $[\eta>10.94,\ \Delta\phi=360.0°]$ and $[8.99>\eta>8.81,\ \Delta\phi=20.0°]$, respectively.

Top panels of Fig.4 present the photon spectra of the combined results of Arm1 and Arm2 together with the predictions by the MC simulations based on different interaction models, DPM-JET 3.04 (red), QGSJET II-03 (blue), SIBYLL 2.1 (green), EPOS 1.99 (magenta) and PYTHIA 8.145 (yellow). In the MC simulations 1.0×10^7 inelastic collisions were simulated with the detector responses using the EPICS/COSMOS libraries, where stochastic fluctuations, e.g. pedestal of DAQ system, are taken into account. Vertical bars and gray hatched areas indicate the experimental statistical and the systematic uncertainties, respectively. The magenta hatched areas show the statistical uncertainty of the MC simulation with EPOS 1.99. Note that the systematic uncertainty of the luminosity determination $\pm6.1\%$ is not included in the figure, since this term only affects the absolute normalization.

Some remarkable features are:

1) DPMJET 3.04 and PYTHIA 8.145 show very good agreement with the experimental result between 0.5 and 1.5 TeV for $\eta>10.94$, but they predict significantly larger photon yield at high energy $>2\,\mathrm{TeV}$ in both rapidity ranges.

2) QGSJET II-03 predicts overall lower photon yield than the experimental result. This is significant above 2 TeV in the rapidity range $8.81<\eta<8.99$.

3) For $\eta>10.94$, SIBYLL 2.1 shows a very good agreement with the experimental result for the spectral shape for $>0.5\,\mathrm{TeV}$, but predicts a photon yield only half of the experimental result over the entire energy range.

8   Results of photon analysis at $\sqrt{s} = 900\,\mathrm{GeV}$

To reduce a possible pseudorapidity η dependence when comparing and combining the energy spectra measured by the two Arms, we selected Arm2 events with a pseudorapidity range similar to that of Arm1. For the small tower, we selected events with the distance r from the beam center less than 11 mm, which corresponded to the pseudorapidity range of $\eta > 10.15$ (the circles in Fig. 2). Similarly, for the large tower, we set the conditions as $22\,\mathrm{mm} < r < 44$ mm, which corresponded to the pseudorapidity range of $8.77 < \eta < 9.46$ (the arcs in Fig. 2). The calorimeters did not uniformly cover the pseudorapidity ranges as shown in Fig. 2. We confirmed that there was a negligible pseudorapidity dependence of the energy spectra inside each pseudorapidity range.

The combined energy spectra of Arm1 and Arm2 are shown in Fig. 5 as weighted averages, with the weights taken to be the square of the inverse of the errors in each energy bin. The error bars of the data (black points) represent the statistical error; the hatches in the spectra
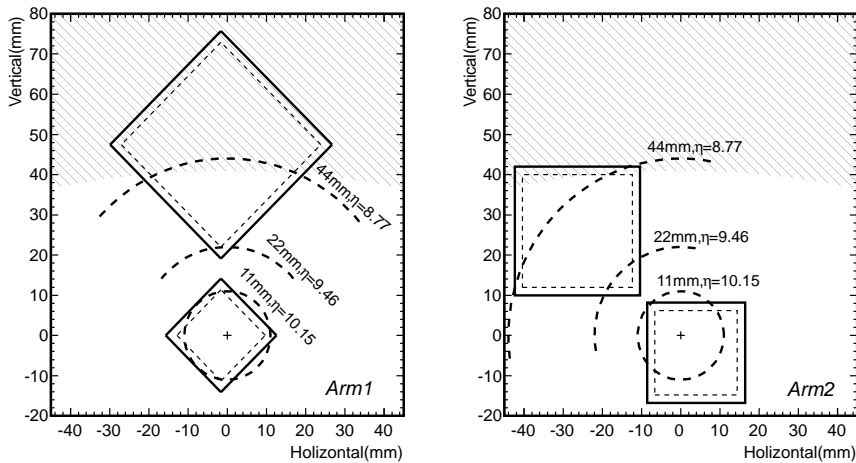
Figure 2: The cross-sections of the calorimeters viewed from IP1, left for Arm1 and right for Arm2. The cross marks on the small calorimeters indicate the projections of the zero-degree collision angle onto the detectors ("beam center"). The shaded areas in the upper parts of the figure indicate the shadows of the beam pipes located between IP1 and the detectors, where the detectors are insensitive to the detection of IP1 proton-proton collision products. The dashed squares indicate the border of a 2 mm edge cut described in Sec. 5.3.

represent the total uncertainty (quadratical summation of the statistical and the systematic errors). The sources of the systematic error are the particle identification and the beam position uncertainties. The energy scale errors were also included, assuming a correlation between the two Arms. Note that the uncertainty of the luminosity determination ($\pm 21\,\%$) is not shown in Fig. 5. It can introduce a constant vertical shift of the spectra, but it cannot change the shapes of the spectra.

In Fig. 5, the predictions of the hadronic interaction models, QGSJET II-03, PYTHIA 8.145, SIBYLL 2.1, EPOS 1.99 and DPMJET 3.04, are also shown. The same analysis processes were applied to the MC simulations as to the experimental data except for the particle identification using $L_{90\%}$ and its correction. For the analysis of the MC simulations, the known particle type was used. For better visibility, only the statistical errors for DPMJET 3.04 (red points) are shown by the error bars.

9 Conclusions

The inclusive production of neutral pions in the rapidity range larger than $y = 8.9$ at $\sqrt{s} = 7\,\text{TeV}$ proton-proton collisions and the forward inclusive photon energy spectra in the pseudorapidity ranges of $\eta > 10.15$ and $8.77 < \eta < 9.46$ for $\sqrt{s} = 900\,\text{GeV}$ proton-proton collisions have been measured by the LHCf experiment in proton-proton collisions at the LHC in early 2010. Transverse momentum spectra of neutral pions and energy spectra of photons have been measured by two independent LHCf detectors, Arm1 and Arm2, and give consistent results.

The combined Arm1 and Arm2 spectra have been compared with the predictions of five hadronic interaction models, DPMJET 3.04, EPOS 1.99, PYTHIA 8.145, QGSJET II-03 and SIBYLL 2.1. For the neutral pion spectra, DPMJET 3.04, EPOS 1.99 and PYTHIA 8.145 agree with the LHCf combined results in general for the rapidity range $9.0 < y < 9.6$ and $p_\text{T} < 0.2\,\text{GeV}$. QGSJET II-03 has poor agreement with LHCf data for $8.9 < y < 9.4$, while it agrees with LHCf data for $y > 9.4$. Among the hadronic interaction models tested in this paper, EPOS 1.99 shows the best overall agreement with the LHCf data even for $y > 9.6$.

For the photon spectra, EPOS 1.99 and SIBYLL 2.1 reproduce well the shape of the experimental energy spectra, but they predict a lower cross section than the LHCf data. The other models predict harder spectra than the LHCf data above $300\,\mathrm{GeV}$. These results of comparison exhibited features similar to those for the previously reported data for $\sqrt{s} = 7\,\mathrm{TeV}$ collisions.
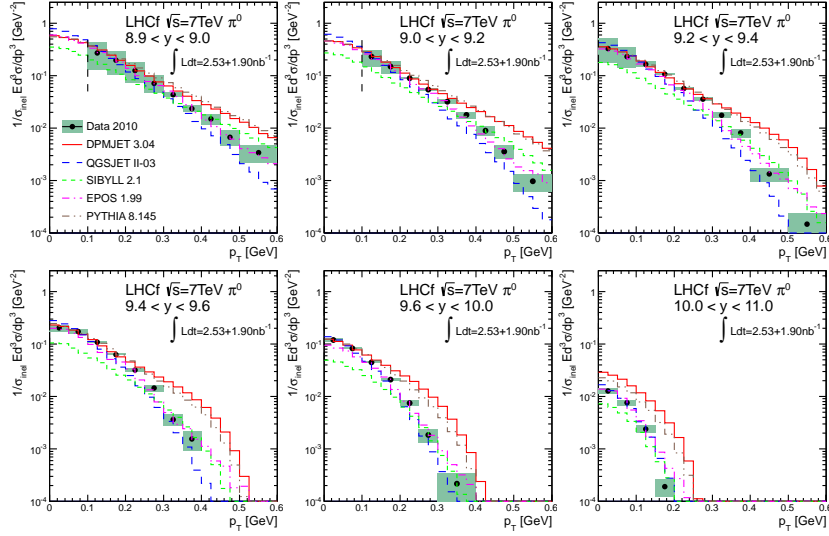

Figure 3: Combined p_T spectra of the Arm1 and Arm2 detectors (black dots) and the total uncertainties (shaded rectangles) compared with the predicted spectra by hadronic interaction models.

References

[1] LHCf Technical Design Report, CERN-LHCC-2006-004

[2] R. Ulrich, R. Engel and M. Unger, Phys. Rev. D **83**, 054026 (2011).

[3] R.D. Parsonsa, C. Bleveb, S.S. Ostapchenko, J. Knappa, Astroparticle Physics **34**, 832-839 (2011).

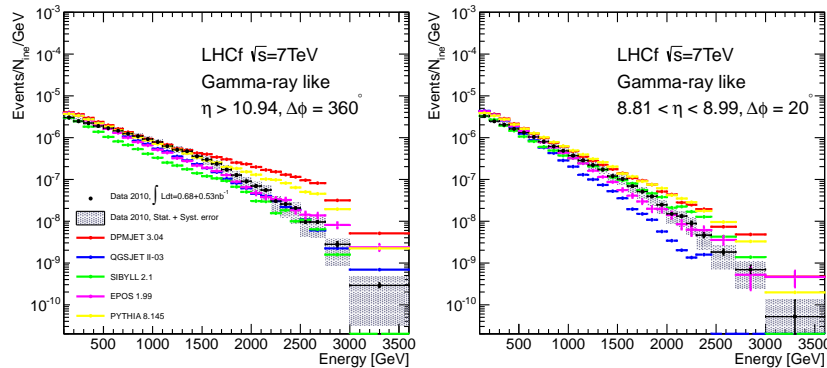[4] J. Abraham, *et al.*, Phys. Rev. Lett., **101** 061101 (2008).

Figure 4: The single-photon energy spectra of the combined experimental data and the MC predictions. Left (right) panel shows the results for the large (small) rapidity range.
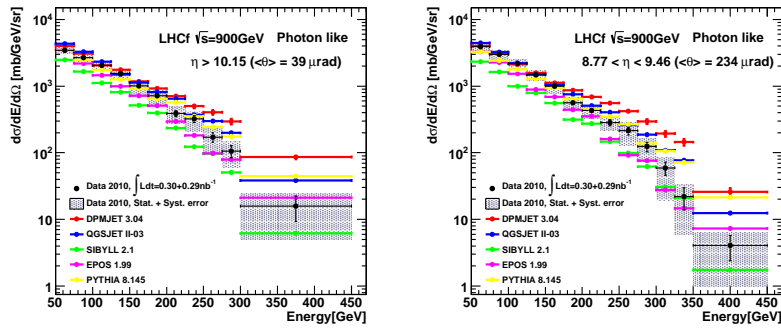
Figure 5: Combined Arm1 and Arm2 photon energy spectra compared with MC predictions. The left and the right panels are the results of the small and the large towers, respectively.

[5] P. Abreu, *et al.*, Astropart. Phys., **34**, 314-326 (2010).

[6] J. Abraham, *et al.*, Phys. Rev. Lett., **104**, 091101 (2010).

[7] R. Abbasi, *et al.*, Astropart. Phys., **32**, 53-60 (2009).

[8] R. U. Abbasi, *et al.*, The Astrophysical Journal Letters, **713**, 64-68 (2010).

[9] R. U. Abbasi, *et al.*, Phys. Rev. Lett. **104**, 161101 (2010).

[10] H. Sagawa, AIPC, **1367**, 17-22, (2011).

[11] W. C. Turner, E. H. Hoyer and N. V. Mokhov, Proc. of EPAC98, Stockholm, 368 (1998). LBNL Rept. LBNL-41964 (1998).

[12] K. Taki, *et al.*, JINST, **7** T01003 (2012).

[13] O. Adriani, *et al.*, Phys. Lett. B **703**, 128-134 (2011).

[14] The ATLAS collaboration, ATLAS-CONF-2010-060.

[15] G. Antchev, *et al.* (The TOTEM Collaboration), EPL **96** 21002 (2011).

[16] K. Nakamura, *et al.*. (Particle Data Group), J. Phys. G 37, 075021 (2010).

[17] K. Kasahara, Proc. of 24th Int. Cosmic Ray. Conf. Rome **1**, 399 (1995). EPICS web page, http://cosmos.n.kanagawa-u.ac.jp/

[18] S. Ostapchenko, Nucl. Phys. Proc. Suppl. **151**, 143 (2006).

[19] F. W. Bopp, J. Ranft, R. Engel and S. Roesler, Phys. Rev. **C77**, 014904 (2008).

[20] E.-J. Ahn, R. Engel, T. K. Gaisser, P.Lipari and T. Stanev, Phys. Rev. **D80**, 094003 (2009).

[21] K. Werner, F.-M. Liu and T. Pierog, Phys. Rev. **C74**, 044902 (2006).

[22] T. Sjöstand, S. Mrenna and P. Skands, JHEP05, 026 (2006).

[23] T. Sjöstand, S. Mrenna and P. Skands, Comput. Phys. Comm., **178**, 852 (2008).

[24] L. D. Landau and I. J. Pomeranchuk, Dokl. Akad. Nauk, **92**, 535-536 (1965).

[25] A. B. Migdal, Phys. Rev. **103**, 1811 (1956).

[26] M. Morhac *et al.*, NIM **A401**, 113-132 (1997), M. Morhac *et al.*, NIM **A401**, 385-408 (1997), M. Morhac *et al.*, NIM **A443**, 108-125 (2000).

[27] Rene Brun and Fons Rademakers, ROOT - An Object Oriented Data Analysis Framework, Proceedings AIHENP'96 Workshop, Lausanne, Sep. 1996, NIM **389**, 81-86 (1997). See also `http://root.cern.ch/`.

[28] F. James and M. Roos, Computer Physics Communications 10 343-367 (1975).

[29] O. Adriani, *et al.*, JINST, **5**, P01012 (2010).

[30] M. Mizuishi *et al.*, J. Phys. Soc. Jpn. **78** (2009) Suppl. A, pp. 173-176.

[31] T. Pierog, Private communication.